

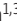
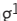






# REPORT

# Primary cilia sensitize endothelial cells to BMP and prevent excessive vascular regression

Anne-Clémence Vion<sup>1,2,3</sup> , Silvanus Alt<sup>1</sup>, Alexandra Klaus-Bergmann<sup>1,3</sup> , Anna Szyborska<sup>1,3</sup> , Tuyu Zheng<sup>1</sup> , Tijana Perovic<sup>1</sup> , Adel Hammoutene<sup>4,5</sup>, Marta Bastos Oliveira<sup>1</sup> , Eireen Bartels-Klein<sup>1,3</sup>, Irene Hollfinger<sup>1</sup>, Pierre-Emmanuel Rautou<sup>4,5,6</sup>, Miguel O. Bernabeu<sup>7,8</sup> , and Holger Gerhardt<sup>1,2,3,9,10,11</sup> 

**Blood flow shapes vascular networks by orchestrating endothelial cell behavior and function. How endothelial cells read and interpret flow-derived signals is poorly understood. Here, we show that endothelial cells in the developing mouse retina form and use luminal primary cilia to stabilize vessel connections selectively in parts of the remodeling vascular plexus experiencing low and intermediate shear stress. Inducible genetic deletion of the essential cilia component intraflagellar transport protein 88 (IFT88) in endothelial cells caused premature and random vessel regression without affecting proliferation, cell cycle progression, or apoptosis. IFT88 mutant cells lacking primary cilia displayed reduced polarization against blood flow, selectively at low and intermediate flow levels, and have a stronger migratory behavior. Molecularly, we identify that primary cilia endow endothelial cells with strongly enhanced sensitivity to bone morphogenetic protein 9 (BMP9), selectively under low flow. We propose that BMP9 signaling cooperates with the primary cilia at low flow to keep immature vessels open before high shear stress-mediated remodeling.**

## Introduction

Efficient oxygen and nutrient supply through the formation of a hierarchically branched network of blood vessels is essential for vertebrate development. A primary vascular plexus initially expands by sprouting angiogenesis (Isogai et al., 2003; Potente et al., 2011) followed by vascular remodeling to adapt vessel organization, shape, and size; in its course, superfluous and inefficient connections are pruned away by active regression (Franco et al., 2015). Mice with genetic inactivation of factors involved in vascular remodeling die during midgestation (Potente et al., 2011), demonstrating the critical importance of remodeling. Nevertheless, the maintenance of redundant collateral vessels, despite being poorly perfused in normal physiology, is critical for recovery after injury; in this context, superfluous connections become active, increase in size, and substitute damaged vessels (Liu et al., 2014). Thus, excessive remodeling and the removal of all nonperfused vessels carry long-term risk, whereas too little remodeling impedes vascular function.

Cells need to respond appropriately to mechanical cues to ensure healthy tissue development and homeostasis.

Endothelial cells (ECs) in particular are under constant mechanical strains exerted by blood flow. Interestingly, ECs are able to sense small variations in the direction, magnitude, and regularity of blood flow-induced shear stress (Wang et al., 2013; Givens and Tzima, 2016) and respond to such changes by influencing vasculature remodeling (Culver and Dickinson, 2010; Baeyens et al., 2016a). Adaptation of ECs to flow is critical for the development and maintenance of a well-functioning cardiovascular system; for example, in adult mice flow-sensing through VEGFR3 controls vessel caliber (Baeyens et al., 2015). However, how ECs sense and transduce mechanical signals during vascular remodeling to achieve a balanced network of blood vessels is still poorly understood (Dolan et al., 2013). Vascular regression has been shown to rely on axial polarization of ECs against the direction of blood flow and their consequent migration from poorly perfused vessels into well-perfused neighboring segments, thus removing superfluous connections and reinforcing vessels that experience higher shear stress (Franco et al., 2015, 2016).

<sup>1</sup>Max Delbrück Center for Molecular Medicine, Berlin, Germany; <sup>2</sup>Vascular Biology Laboratory, London Research Institute – Cancer Research UK, Lincoln's Inn Fields Laboratories, London, England, UK; <sup>3</sup>German Center for Cardiovascular Research, Berlin, Germany; <sup>4</sup>Institut National de la Santé et de la Recherche Médicale, U970, Paris Cardiovascular Research Center, Paris, France; <sup>5</sup>Université Paris Descartes, Sorbonne Paris Cité, Paris, France; <sup>6</sup>Département Hospitalo-Universitaire Unity, Pôle des Maladies de l'Appareil Digestif, Service d'Hépatologie, Centre de Référence des Maladies Vasculaires du Foie, Hôpital Beaujon, Assistance Publique – Hôpitaux de Paris, Clichy, France; <sup>7</sup>Centre for Medical Informatics, Usher Institute, University of Edinburgh, Edinburgh, Scotland, UK; <sup>8</sup>Centre for Computational Science, Department of Chemistry, University College London, London, England, UK; <sup>9</sup>Vascular Patterning Laboratory, VIB Center for Cancer Biology, Leuven, Belgium; <sup>10</sup>Vascular Patterning Laboratory, Department of Oncology, KU Leuven, Leuven, Belgium; <sup>11</sup>Berlin Institute of Health, Berlin, Germany.

Correspondence to Holger Gerhardt: [holger.gerhardt@mdc-berlin.de](mailto:holger.gerhardt@mdc-berlin.de); Anne-Clemence Vion: [anne-clemence.vion@mdc-berlin.de](mailto:anne-clemence.vion@mdc-berlin.de).

© 2018 Vion et al. This article is distributed under the terms of an Attribution–Noncommercial–Share Alike–No Mirror Sites license for the first six months after the publication date (see <http://www.rupress.org/terms/>). After six months it is available under a Creative Commons License (Attribution–Noncommercial–Share Alike 4.0 International license, as described at <https://creativecommons.org/licenses/by-nc-sa/4.0/>).

Many structures and receptors have been identified as flow sensors in ECs (Traub and Berk, 1998; Baeyens et al., 2016a). Among them, the primary cilium has been shown to bend in response to blood flow and to be required for flow sensing, thus controlling endothelial function in both normal and pathological conditions (Goetz et al., 2014; Dinsmore and Reiter, 2016). The primary cilium extends from the membrane of the cell and is stabilized by a microtubule scaffold known as the axoneme. The ciliary axoneme is surrounded by the ciliary membrane, a specialized compartment in which many receptors, ion channels, and transporter proteins are embedded, where they recruit second messengers and effectors (Satir et al., 2010). Several intraflagellar transport proteins, including intraflagellar transport protein 88 (IFT88), specific kinesin motors like KIF3a, and other structural components like ARL13b, are essential for formation and maintenance of primary cilia (Nonaka et al., 1998; Taulman et al., 2001; Hori et al., 2008). Their selective deletion has been useful to investigate the role of primary cilia in many cells. However, some cilia independent functions can also be found for IFT88 and KIF3a (Delaval et al., 2011; Boehlke et al., 2013, 2015; Borovina and Ciruna, 2013). In blood vessels, the endothelial primary cilium extends into the lumen of the vessels. Activation of the primary cilium by flow triggers calcium signaling and nitric oxide production in vitro (Nauli et al., 2008). In adult mice, loss of endothelial primary cilia aggravates atherosclerosis caused by reduced nitric oxide synthase activity (Dinsmore and Reiter, 2016). In zebrafish embryos, the primary cilium acts as a mechanical sensor for ECs exposed to low shear stress (LSS; Goetz et al., 2014) and contributes to blood–brain barrier integrity (Kallakuri et al., 2015). Finally, the maintenance of cilia has been described to be dependent on flow (Iomini et al., 2004). During valve formation, for example, extreme high shear stress (HSS) levels disrupt cilia, leading to mesenchymal transition through activation of TGF $\beta$ /ALK5 signaling (Ten Dijke et al., 2012). Interestingly, in other cell types, the primary cilium has been shown to transmit signals coming from the Notch, TGF $\beta$ , and Wnt pathways (Goetz and Anderson, 2010; Gerhardt et al., 2016; Pedersen et al., 2016) by allowing the clustering of kinases and their targets. Additionally, hair cells forming the cochlea require a primary cilium to specifically position their basal body on one side of the nucleus, and therefore polarize (Jones et al., 2008).

ECs are highly responsive to bone morphogenetic proteins (BMPs) and TGF $\beta$ , which share common effectors and engage in signaling cross talk (Guo and Wang, 2009). Recent studies reveal that the BMP pathway is important for flow-induced responses through SMAD1/5/8 activity (Zhou et al., 2012; Laux et al., 2013; Baeyens et al., 2016b). SMAD1/5 activation downstream of BMP receptors can be induced by flow in the absence of ligand suggesting a direct effect of mechanical forces on the BMP receptors (Zhou et al., 2012). In zebrafish, the BMP receptor ALK1, responsible for SMAD1/5/8 phosphorylation, has been shown to trigger a flow-sensitive BMP10 response (Laux et al., 2013) contributing to EC migration against the blood flow (Rochon et al., 2016). Latest studies identified that BMP9/10-induced signaling upon HSS stimulation is dependent on the coreceptor Endoglin (Baeyens et al., 2016b).

Here, we demonstrate that IFT88 and most likely the endothelial primary cilium are essential for appropriate vascular patterning by protecting nascent blood vessels exposed to LSS from premature regression. Mechanistically, we show that ECs with primary cilia show strongly enhanced BMP9–Smad1/5/8 signaling selectively when exposed to LSS.

## Results

### Presence of endothelial primary cilia inversely correlates with shear stress levels during vascular remodeling

To assess the distribution of primary cilia in the developing vasculature of the mouse retina, we used immunofluorescence staining for ARL13b. We identified cilia localizing within vascular staining and close to endothelial nuclei (Fig. 1 A) distributed across all parts of the vascular plexus (Fig. 1, B and C), except in tip cells at the sprouting front. Quantification in arteries, veins, and plexus at different developmental stages showed that the number of ECs with primary cilia decreased in arteries as the vasculature developed (Fig. 1, B and C). In vitro, in confluent monolayers of human umbilical vein endothelial cells (HUVECs), ~15% of cells showed an apical primary cilium under static conditions. This percentage decreased with increasing shear stress levels, dropping to 5% under HSS (Fig. 1 D). To investigate potential population dynamics of ECs with cilia, we studied a zebrafish line expressing a membrane reporter for ECs and GFP-tagged ARL13b (Tg(kdr-l:ras-Cherry916;  $\beta$ -actin::arl13b-eGfp)). Although most of the luminal cilia in ECs were stable over the acquisition time (Video 1, 6 h), we identified several appearing (Fig. 1, E and F; and Video 2) or retracting cilia (Fig. 1, E and F; and Video 3). Using adenoviral expression of GFP-tagged ARL13b in HUVECs, we confirmed that only a fraction of ECs (10%) harbored a primary cilium (Fig. S1, A and B). Time-lapse imaging revealed that most of the ciliated cells remained so over the 5-h observation time (Video 4; and Fig. S1, B and C) although, as in zebrafish, some cilia retracted and others appeared de novo (Fig. S1, B and C).

### Primary cilia prevent vascular regression by maintaining collective polarization of ECs

To assess the function of endothelial primary cilia in the retinal vasculature, we performed genetic deletion of *Ift88* specifically in ECs. To do so, we bred mice expressing a tamoxifen-inducible Cre recombinase under the control of the endothelial-specific promoter of *Pdgfrb* (*Pdgfrb-iCre-ERT2-Egfp*; Claxton et al., 2008) with mice expressing floxed alleles of *Ift88* (Haycraft et al., 2007). *Ift88*<sup>fl/fl</sup>; *Pdgfrb-iCre-ERT2-Egfp*<sup>+/wt</sup> offspring were then injected with tamoxifen at postnatal day 1 (P1) and P3 to induce recombination of the floxed alleles (referred to as IFT88 iEC-KO). Western blot analyses on lung ECs, quantitative PCR on retinal ECs, and immunofluorescence staining of retinas confirmed deletion of IFT88 and the loss of primary cilia, respectively (Fig. S1, D–F).

At P6, IFT88 iEC-KO mice showed decreased radial expansion of the retinal vasculature (Fig. 2 A), decreased vascular density (Fig. 2 B), and fewer sprouting cells at the front of the plexus (Fig. 2 C) compared with littermate controls. This phenotype was transient as retinas from P15 mice recovered from the decrease in radial expansion and vascular density (Fig. S1 G).

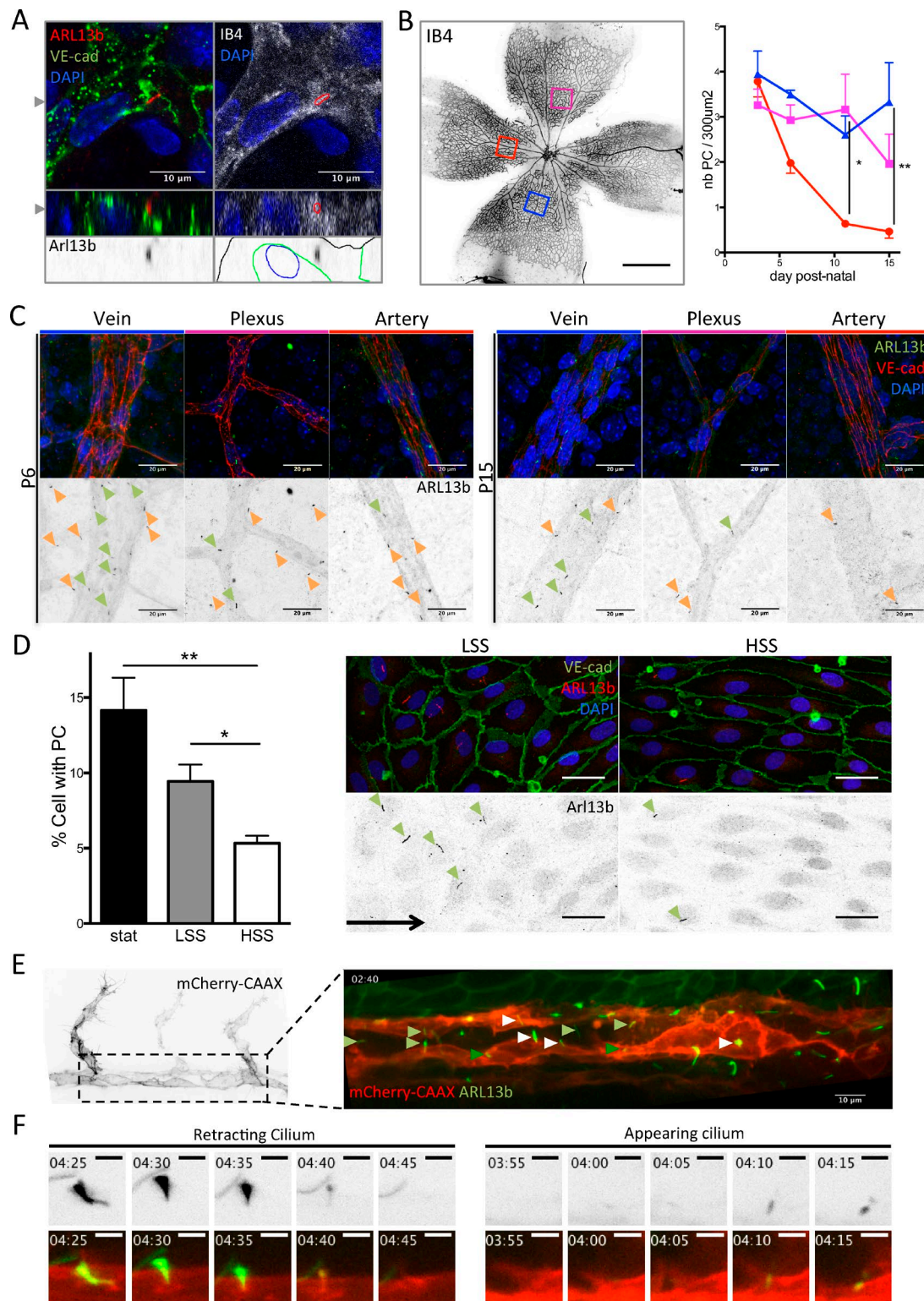


**Figure 1. Primary cilia are present in ECs, and their presence correlates with shear stress levels. (A)** Primary cilia belonging to ECs were found in the retinal vasculature. Top images present one z-stack (depth 0.26 µm) showing the cilium within the vasculature and overlapping with Isolectin staining (red outline on the right upper image highlights the cilium localization). Bottom images present the corresponding z-projection showing the cilium embedded in the endothelial layer (black outline, Isolectin B4; blue outline, DAPI; green outline, VE-cadherin). The gray arrowheads indicate the cut-planes corresponding to the z-stack visualization. **(B)** Retinas from mouse pups were collected at P3, P6, P11, and P15 and stained for VE-cadherin (EC junctions), ARL13b (primary cilia), and DAPI (nuclei). The number of primary cilia present in the different areas of the vasculature was quantified over time and maturation of the vessels in different animals (red, artery; magenta, plexus; blue, vein;  $n = 3$  for each time point; median  $\pm$  interquartile range (IQ); two-way ANOVA. Data distribution was assumed to be normal but this was not formally tested). Bar, 700 µm. **(C)** Representative images are shown for each region. Green arrowheads, endothelial



IFT88 is implicated in spindle orientation in HeLa and epithelial cells (Delaval et al., 2011; Taulet et al., 2017) and is required for orienting cell divisions during gastrulation (Borovina and Ciruna, 2013). Using flow cytometry and propidium iodide staining, we investigated whether ECs lacking IFT88 exhibit cell cycle-related defects or increased apoptosis, two possible causes for reduced vascular density. We found no changes in the proportion of ECs undergoing apoptosis in retinas of iEC-IFT88 mice compared with controls (Fig. S2 A). We confirmed these results by staining retinas for cleaved caspase-3 (Fig. S2 B). The percentage of polyploid ECs and of ECs in G2-M was not increased, suggesting that IFT88 expression levels do not interfere with the final steps of cell division (Fig. S2 A). In contrast, the proportion of ECs in G0-G1 was increased, whereas ECs in S phase were decreased in IFT88 iEC-KO mice compared with controls. However, we found that the proportion of ECs incorporating 5-ethynyl-2'-deoxyuridine (EdU) was increased in IFT88 iEC-KO retinas (Fig. S2 D), suggesting that these cells may remain in S phase for a longer period of time. Nevertheless, the number of ECs forming the retinal vasculature in the remodeling area at P6 was not different between IFT88 iEC-KO and control mice (Fig. S2 C), arguing against a role of proliferation or cell number in regulating vascular density.

As previously described, the ultimate density of the retinal vasculature is regulated by vascular regression (Franco et al., 2015). In retinas, lumen loss (visualized by intercellular adhesion molecule 2 [ICAM2] staining) and the presence of empty collagen sleeves are indicators of vascular regression. We observed that IFT88 iEC-KO retinas showed significantly more collapsed lumens (Fig. 3 A) and more empty collagen sleeves than controls (Fig. 3 B), suggesting that the decrease in vascular density observed in IFT88 iEC-KO mice is caused by increased regression of preexisting vessels. Interestingly, by analyzing the distribution of empty sleeves throughout the retina between vein and artery (Fig. 3 C), we found that vessels in IFT88 iEC-KO retinas preferentially regressed close to veins, whereas vessels in control retinas preferentially regressed close to arteries (Fig. 3 D).

Previous work identified that vascular regression is regulated by blood flow (Chen et al., 2012; Udan et al., 2013). Above a critical threshold, flow induces axial polarization and migration of ECs against the flow direction. In vessel segments exposed to low or discontinuous flow, ECs migrate away from each other into adjacent vessels experiencing higher flow, leading to the regression of the low-flow segment (Franco et al., 2015). To understand the influence of the loss of endothelial primary cilia on vessel stability and regression, we evaluated the flow pattern and polarity profiles in IFT88 iEC-KO retinas, combining in silico simulation

of blood flow patterns (Bernabeu et al., 2014, 2017 Preprint) and in vivo polarity data (assessed by Golgi-nucleus axis direction; Fig. S2 E, white arrows). The overall flow simulation pattern was similar between control and IFT88 iEC-KO retinas (Fig. S2 F). By correlating local shear stress values obtained from these simulations with axial polarity of the ECs in the same retinas, we found that ECs in IFT88 iEC-KO retinas showed similar polarity profiles as those in control retinas, both in regions of LSS and HSS (Fig. 3 E). However, in areas of intermediate shear stress, polarization against the flow was significantly reduced in ECs of IFT88 iEC-KO retinas compared with controls (Fig. 3 E). Interestingly, this range of shear stress prevailed precisely in the areas of increased regression in IFT88 iEC-KO retinas (Fig. 3 F). We further manually quantified the number of vessel segments displaying two or more ECs oriented in opposite directions (referred to as divergent polarity; Fig. 3 G). Localization of these events was shifted significantly toward veins in IFT88 iEC-KO retinas (Fig. 3 H). Together, the loss of flow-induced polarity and increased regression preferentially in LSS areas (i.e., close to veins) suggest that IFT88, very likely by supporting cilia formation, contributes to flow sensing and vessel maintenance in poorly perfused segments.

### Primary cilium augments BMP9 responses in ECs and decreases their migration speed

In search for the cellular and molecular mechanisms under control of the primary cilium in ECs, we silenced IFT88 in HUVECs using siRNAs (Fig. S3 A), reducing the number of primary cilia by 75% (Fig. S3 B). As the basal body of the primary cilium has been shown in different cell types to be required for the activation of several signaling pathways (Goetz and Anderson, 2010; Gerhardt et al., 2016; Pedersen et al., 2016) as well as the inhibition of the BMP7 pathway (Fuentealba et al., 2007), we asked whether IFT88 silencing in ECs affected these pathways under LSS using quantitative PCR for downstream targets. First, we observed that the BMP pathway (*SMAD6*) was highly up-regulated by LSS (Fig. 4 A). *TGF $\beta$*  (*SERPIN1*) and Notch (*HES1*) pathways were also up-regulated, but to lesser extent than BMP. As in other cell types, *PTCH1* expression, a reference gene for activation of the SHH pathway, was significantly decreased (Fig. 4 A). Although Notch, *TGF $\beta$* , and Wnt (*AXIN2*) signaling appeared unchanged (Fig. 4 A), BMP signaling was significantly decreased in IFT88-deficient ECs compared with controls (Fig. 4 A). Further, we investigated whether IFT88-deficient cells were still responsive to BMP9 stimulation. Both *ID1* and *SMAD6* expression were up-regulated by BMP9 stimulation (25 pg/ml) in control cells (8- and 20-fold, respectively) but were reduced

primary cilia; orange arrowheads, primary cilia from surrounding cells. Bars, 20  $\mu$ m. (D) Monolayers of HUVECs were subjected to different shear stress conditions for 24 h ( $n = 8$ ; mean  $\pm$  SEM; two-sided Wilcoxon test) and then stained for VE-cadherin, ARL13b (primary cilia), and DAPI. The percentage of cells with a PC within the monolayers was quantified. Representative images are shown for static (stat) and HSS conditions. Green arrowheads, endothelial primary cilia; black arrow, flow direction. Bars, 20  $\mu$ m. (E) A 24- to 30-hpf zebrafish embryo of double transgenic line Tg(kdr:lras-Cherry916;  $\beta$ -actin::arl13b-eGfp) was used to identify the dynamics of endothelial cilia over time. First image shows the EC labeling (referred to as mCherry-CAAX). Second image shows the luminal cilia (white arrowhead, disappearing cilia; light green arrowhead, stable cilia; dark green arrowhead, appearing cilia). Movie of the cilia dynamics is provided in Video 1. Bar, 10  $\mu$ m. (F) Stills extracted from Videos 2 and 3 showing the retraction of the cilium ("retracting cilium") or its formation ("appearing cilium"). Bars, 3  $\mu$ m. \*,  $P < 0.05$ ; \*\*,  $P < 0.01$ . PC, primary cilium.

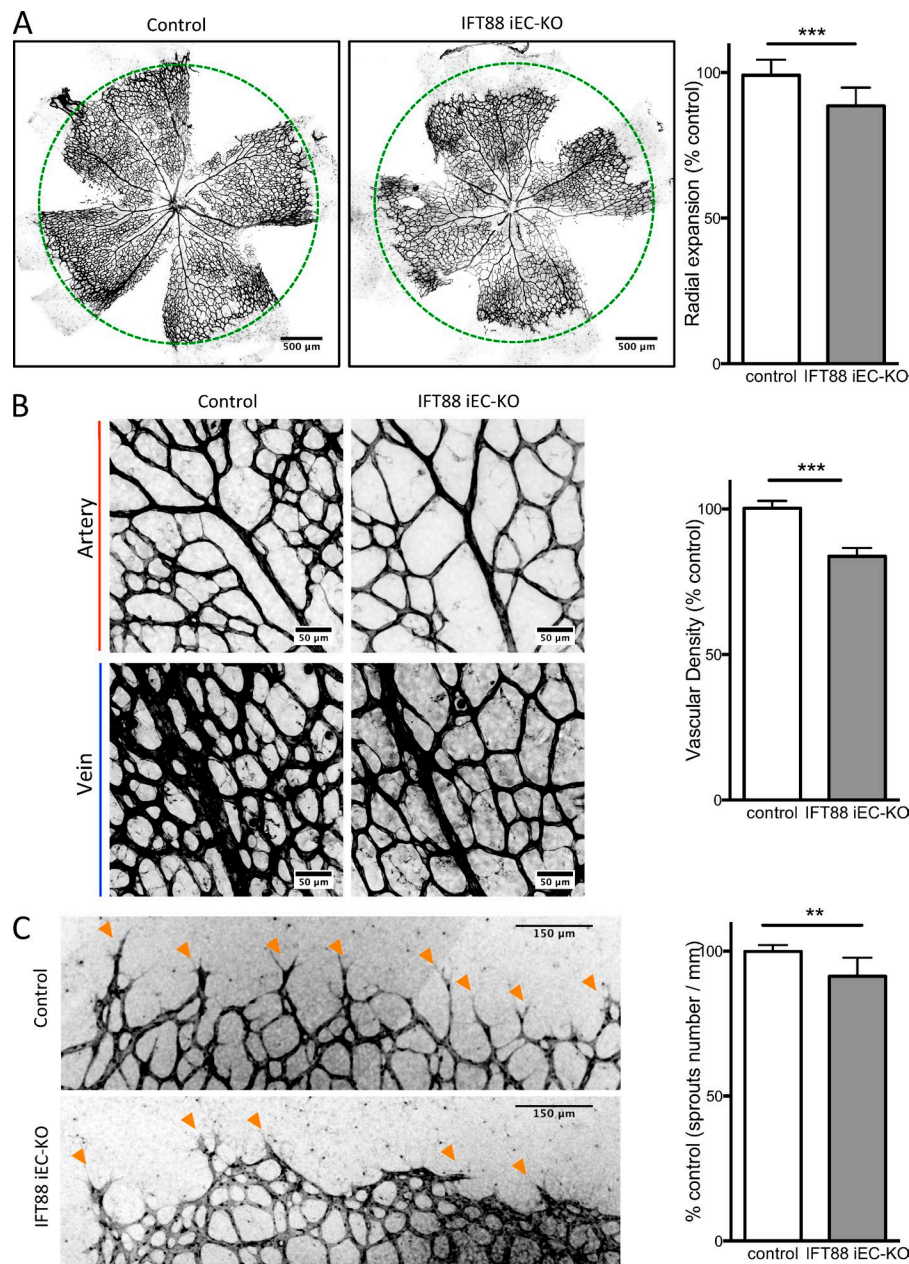


**Figure 2. IFT88 iEC-KO mice show defects in vascular expansion and density.** *Ift88<sup>fl/fl</sup>;Pdgfr- $\alpha$ -Cre-ERT2-Egfp<sup>+/wt</sup>* (IFT88 iEC-KO) and littermate mice (control) were injected with tamoxifen at P1 and P3 and eyes collected at P6. **(A)** Representative images of retinal wholemounts stained with Isolectin B4 (IB4, black; green circles represent the radial expansion in control mice) and quantification of the radial expansion of the vascular plexus in IFT88 iEC-KO mice and littermate controls (WT,  $n = 9$ ; KO,  $n = 12$ ; median  $\pm$  IQ; two-sided Wilcoxon test). **(B)** Representative images (black, IB4) and quantification of vascular density of the plexus in IFT88 iEC-KO mice and littermate controls (expressed as vascularized area normalized to control situation; WT,  $n = 5$ ; KO,  $n = 9$ ; median  $\pm$  IQ; two-sided Wilcoxon test). **(C)** Representative images (black, IB4) and quantification of the number of sprouting cells (orange arrowheads) in IFT88 iEC-KO mice and littermate controls (WT,  $n = 6$ ; KO,  $n = 5$ ; median  $\pm$  IQ; two-sided Wilcoxon test). \*\*,  $P < 0.01$ ; \*\*\*,  $P < 0.001$ .

by 50% after IFT88 silencing (Fig. S3 C). To understand if this was related to a specific range of shear stress, we evaluated the response of ECs to BMP9 under different shear stress conditions (Fig. 4, B and C; and Fig. S3, D–F). A recent study demonstrated that HUVECs exposed to shear stress show increased sensitivity to BMP9 (Baeyens et al., 2016b). Indeed, when repeating the very same dose–response study using semiquantitative Western blot analysis of phospho-SMAD1/5/8 (p-SMAD1/5/8) levels, we confirmed the dramatic increase in the sensitivity of ECs to BMP9 stimulation when exposed to shear stress compared with static conditions. Surprisingly, however, this effect was much more pronounced at LSS values (not tested in Baeyens et al., 2016b). We identified a half-maximal effective concentration (EC50) of BMP9 of 1.26 pg/ml for ECs under LSS compared with 9.27 pg/ml for ECs under HSS and 38.44 pg/ml for the static condition (Fig. 4, B and C; and Fig. S3, D–F). Intriguingly, IFT88-deficient

cells completely lost this differential response to LSS and HSS, displaying very similar sensitivities to BMP9 with values comparable to control cells under HSS ( $EC_{50}^{low\ shear\ IFT88} = 10.61\text{ pg/ml}$ ;  $EC_{50}^{high\ shear\ IFT88} = 7.89\text{ pg/ml}$ ; Fig. 4, B and C; and Fig. S3, D–F). These results demonstrate that IFT88, likely by supporting formation of the primary cilium, equips ECs with a sharp sensitivity to BMP9, selectively at LSS levels. Surprisingly, although further increases in BMP9 levels eventually caused signal saturation, only control cells exposed to LSS desensitized at the highest concentrations of BMP9, as indicated by a drop in p-SMAD1/5/8 levels (Fig. 4, B and C; and Fig. S3, E and F). Together, this suggests that ECs capable of forming a primary cilium are highly sensitive to BMP9 with a unique dose–response curve at LSS values.

The activation of downstream target genes by p-SMAD1/5/8 requires their translocation to the nucleus. We therefore analyzed nuclear translocation of p-SMAD1/5/8 by immunostaining at



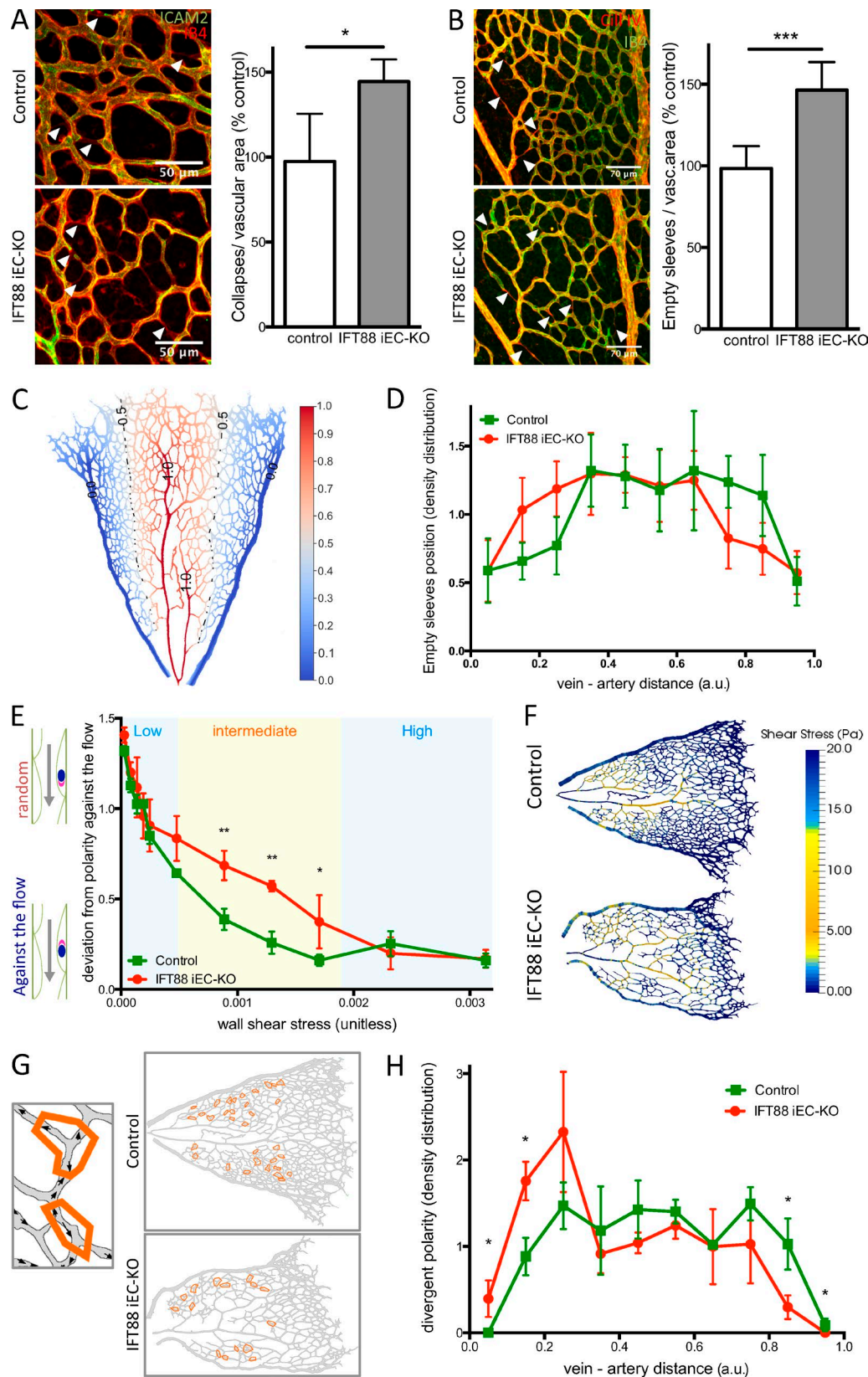


**Figure 3. IFT88 iEC-KO mice show increased random vascular regression and loss of flow-induced polarity.** (A) Retinas from P6 IFT88 iEC-KO and littermate control mice were stained for ICAM2 (green) and with Isolectin B4 (red). Arrowheads show collapsed vessels. The number of collapsed lumens per vascular area was quantified in both groups ( $n = 8$ ; median  $\pm$  IQ; two-sided Wilcoxon test; \*,  $P < 0.05$ ). Bars, 50  $\mu\text{m}$ . (B) Retinas from P6 IFT88 iEC-KO and littermate control mice were stained for Collagen IV (red) and with Isolectin B4 (green). Arrowheads show collagen empty sleeves. The number of empty sleeves

different levels of shear stress. Stimulation with 10 pg/ml BMP9 strongly triggered translocation of p-SMAD1/5/8 to the nucleus in control cells in all shear stress conditions and at a higher rate at LSS and HSS levels (5.8- and 4.5-fold, respectively; Fig. 4 D) compared with static conditions (1.7-fold; not depicted). Interestingly, the pronounced translocation of p-SMAD1/5/8 after BMP9 stimulation under LSS was abolished upon silencing of IFT88. In contrast, IFT88-deficient ECs exposed to HSS remained responsive to BMP9 stimulation, but at lower levels than control cells (3.6-fold increase instead of 4.5-fold; Fig. 4 D). Because IFT88 has been shown to have cilium-independent roles (Delaval et al., 2011; Boehlke et al., 2015; Taulet et al., 2017), we evaluated the effect of KIF3a silencing, another key protein in cilium maintenance, on BMP signaling. First, we confirmed by qPCR that ECs expressing shRNA targeting KIF3a was effective (Fig. S3 G). This silencing led to a decrease in SHH activity (*PTCH1* and *GLII*), as expected from the loss of the primary cilium (Fig. S3 G). Similar to the IFT88 silencing experiment, both *ID1* and *SMAD6* gene expression were up-regulated by 25 pg/ml BMP9 stimulation in control ECs (four- and fivefold, respectively) but were reduced by 40% after KIF3a silencing (Fig. S3 H). Additionally, LSS-induced translocation of p-SMAD1/5/8 into the nucleus was abolished in KIF3a-deficient ECs, whereas HSS-induced translocation was maintained (Fig. 4 E). These results suggest that in ECs, the ability to form primary cilia is critical for both SMAD1/5/8 phosphorylation and nuclear translocation under LSS, but not under HSS.

Furthermore, staining for p-SMAD1/5/8 in the retina confirmed this observation; in the remodeling area p-SMAD1/5/8 was decreased in endothelial nuclei in the IFT88 iEC-KO mice compared with controls (Fig. 4 F). Expression of *Smad6* and *Serp11* was also reduced in ECs extracted from IFT88 iEC-KO retinas (Fig. 4 G) but the expression levels of receptors for BMP9 or TGF $\beta$  (*Alk1* and *Alk5*) and the coreceptor Endoglin (*Eng*) were unchanged (Fig. 4 G). Interestingly, in vitro, ALK1 appears enriched around the cilium in ciliated ECs (Fig. 5 A); this specific localization close to the Golgi was reduced in nonciliated ECs (Fig. 5 A). We also identified prominent phosphorylation of SMAD1/5/8 at the basal body and along the cilium (Fig. 5 B) as well as SMAD4 localization along the cilium (Fig. 5 C) upon LSS stimulation in vitro.

BMP9/10 signaling through ALK1 has been proposed as a regulator of vascular remodeling by stimulating cell migration against the flow and promoting EC quiescence in zebrafish (Laux et al., 2013; Rochon et al., 2016). Given previous studies that directional migration is a key factor during vascular regression (Franco et al., 2015), we asked whether migration was affected

by IFT88 loss. Interestingly, Both IFT88-deficient and KIF3a-deficient ECs migrated significantly faster than control cells to close a scratch wound in vitro (Fig. 5, D and E). Trapping BMP9 in the medium using the ALK1-Fc receptor-body equally accelerated wound closure of control cells but had no additional effect on KIF3a-deficient ECs or IFT88-deficient ECs (Fig. 5, D and E). These data highly suggest that BMP9 signaling is responsible for the decreased migration in ECs capable of forming a primary cilium. Finally, IFT88-deficient ECs, KIF3a-deficient ECs, and ALK1-Fc receptor body-treated ECs harbored significantly more ECs with a long and continuous lamellipodium along the free edge of the wound (Fig. 5, E and F). Such lamellipodia correlate with higher speed of migration in other cell types (Lee et al., 1993) and point toward changes in cytoskeletal organization during migration as a potential downstream target of BMP signaling through IFT88 and KIF3a and hence likely through the primary cilium.

## Discussion

Our present results identify that ECs display primary cilia in a temporal and spatial pattern that correlates with particular hemodynamic settings during vascular remodeling in the mouse retina. Similar to earlier observations in the developing zebrafish embryo (Goetz et al., 2014), we find primary cilia most frequently in ECs exposed to LSS and moderate shear stress, whereas most cells exposed to HSS do not show a cilium. This corroborates several studies demonstrating that HSS disrupts endothelial primary cilia (Iomini et al., 2004; Egorova et al., 2011; Ten Dijke et al., 2012). We show that even at lower shear values, cilia dynamically form and disappear, suggesting that ECs may experience differential or recurring phases of cilia expression during vascular development. Dinsmore and Reiter (2016) reported that genetic constitutive deletion of IFT88 in ECs has no effect on the vasculature of the retina in newborns but causes the formation of large atherosclerotic lesions in turbulent/LSS areas of the aorta. In our present work, we find that inducible genetic deletion of primary cilia in ECs during postnatal retina development causes premature and widespread vessel regression.

Morphological telltale signs of apical shear forces experienced by ECs are their elongated morphology and the polarized positioning of their Golgi and centrosome ahead of the nucleus, against the direction of flow (Vyalov et al., 1996). Accumulating evidence indicates that this axial polarity coincides with directional cell migration against the flow (Ostrowski et al., 2014; Franco et al., 2015; Rochon et al., 2016). Combined simulation of hemodynamics (Bernabeu et al., 2014) and analysis of axial

was quantified in both groups (WT,  $n = 9$ ; KO,  $n = 7$ ; median  $\pm$  IQ; two-sided Wilcoxon test; \*\*\*,  $P < 0.001$ ). Bars, 70  $\mu$ m. (C) Representation of the method determining the distance value for elements placed between a vein and an artery (0 = touching the vein, 1 = touching the artery). (D) The distribution of empty sleeves was quantified in IFT88 iEC-KO mice and littermate controls (WT,  $n = 9$ ; KO,  $n = 7$ ; mean  $\pm$  SEM; one-sided Mann-Whitney  $U$  test). (E) Flow-induced polarity profile depending on shear stress value in the retina of the IFT88 iEC-KO mice compared with littermate controls ( $n = 3$ ; mean  $\pm$  SEM; 0 = perfect polarity against the flow direction; 1.6 = random polarity; one-sided Mann-Whitney  $U$  test; \*,  $P < 0.10$ ; \*\*,  $P < 0.05$ ). (F) Visualization of simulated shear profiles in P6 IFT88 iEC-KO and littermate control retinas. The color-coding is adjusted to highlight the intermediate shear range where ECs in the KO show reduced polarity (shown in yellow, representative images of six animals). (G) Schematics showing examples of divergent polarity events in the remodelling plexus. Arrows, polarity vectors; orange contours, regions of divergent polarity. (H) The density distribution of divergent polarity events was determined for both IFT88 iEC-KO mice and littermate controls ( $n = 3$ ; mean  $\pm$  SEM; one-sided Mann-Whitney  $U$  test; \*,  $P < 0.10$ ; \*\*,  $P < 0.05$ ). a.u., arbitrary unit.

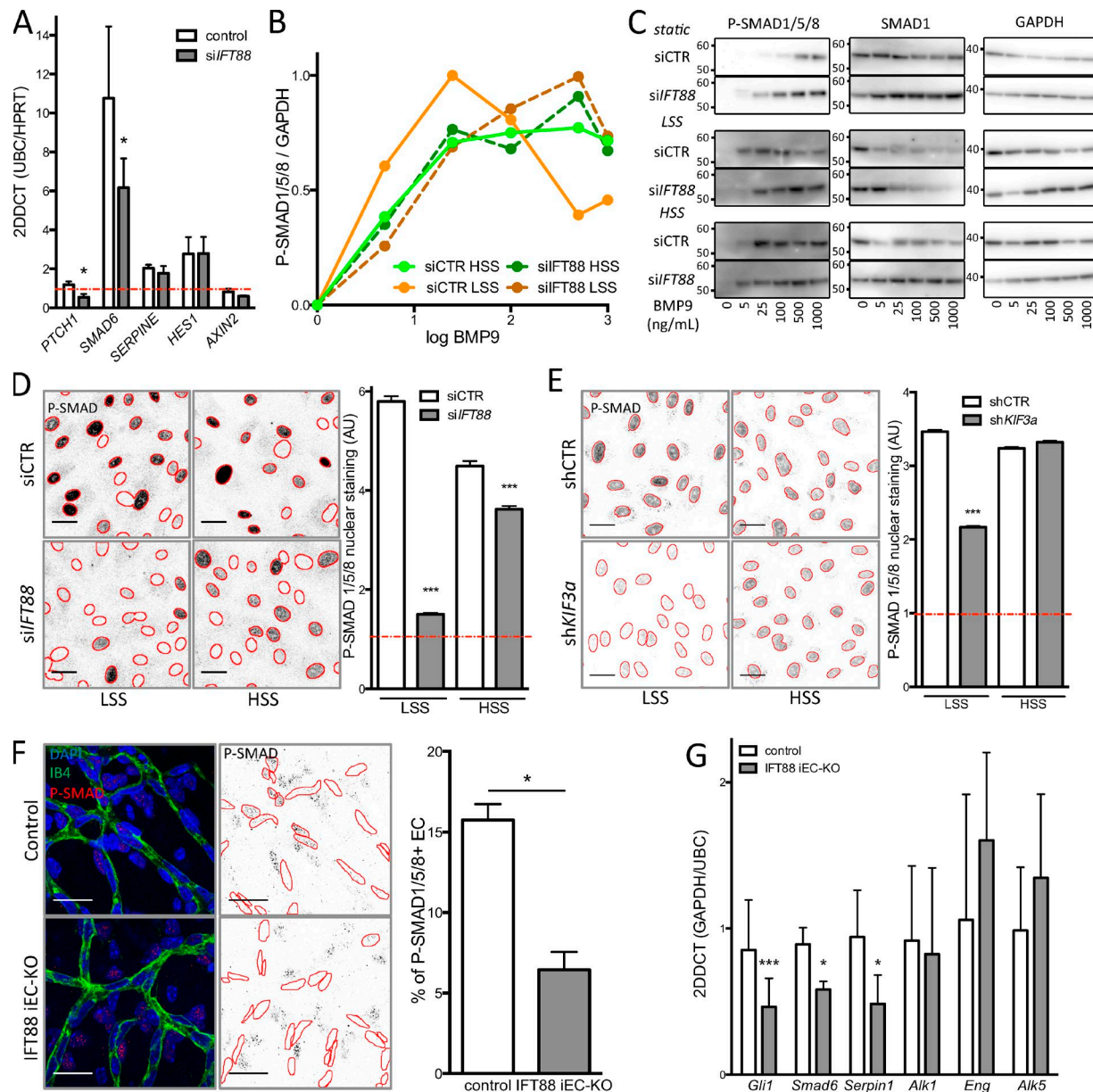


**Figure 4. Loss of the primary cilium leads to increased migration and blocks the differential response to BMP9 under flow.** (A) quantitative PCR was used to assess levels of SHH (*PTCH1*), BMP (*SMAD6*), TGF $\beta$  (*SERPINE*), Notch (*HES1*), and Wnt (*AXIN2*) signaling in ECs transfected with siIFT88 or siCTR under LSS conditions ( $n = 5$ ; all conditions were normalized to 1 for siCTR under the static condition [red line,  $n = 4$ ]; mean  $\pm$  SEM; two-sided Wilcoxon test; \*,  $P < 0.05$ ). (B) Dose-response curves were generated for p-SMAD1/5/8 levels after BMP9 stimulation based on Western blot analysis ( $n = 3$ ; mean: LSS = 2 dyn/cm $^2$ ; HSS = 20 dyn/cm $^2$ ). (C) Representative images of the Western blots used for the dose-response analysis. Molecular masses are indicated on the images based on prestained protein standard. (D) Representative images (red outline based on DAPI segmentation) and quantification of p-SMAD1/5/8 nuclear staining (PFA fixation) in ECs transfected with siCTR or siIFT88 and treated with 10 pg/ml BMP9 (the red line represents nontreated cell level of staining;  $n = 3$ ; between 1,900 and 3,300 cells per condition; mean  $\pm$  SEM [of cell individual values]; two-sided Mann-Whitney  $U$  test; \*\*\*,  $P < 0.001$ ). Bars, 30  $\mu$ m. (E) Representative images and quantification of p-SMAD1/5/8 nuclear staining (PFA fixation) in ECs transfected with shCTR or shKIF3a and treated with 10 pg/ml BMP9 (the red line represents nontreated cell level of staining;  $n = 3$ ; between 1,900 and 3,300 cells per condition; mean  $\pm$  SEM [of cell individual values]; two-sided Mann-Whitney  $U$  test; \*\*\*,  $P < 0.001$ ). Bars, 30  $\mu$ m. (F) Representative images of immunofluorescent staining of p-SMAD1/5/8 in the retina of IFT88 IEC-KO mice or littermate control and quantification of the nuclear signal in ECs. Positive staining in surrounding cells is still visible in the IFT88 IEC-KO retina (control,  $n = 5$ ; IFT88 IEC-KO,  $n = 7$ , blue: DAPI; red: p-SMAD1/5/8; green: Isolectin; mean  $\pm$  SEM; two-sided Wilcoxon test; \*,  $P < 0.05$ ). Bars, 20  $\mu$ m. (G) qPCR analysis was performed on ECs extracted from IFT88 IEC-KO (gray) and littermate retinas (white;  $n = 7$ ; mean  $\pm$  SEM; two-sided Wilcoxon test; \*,  $P < 0.05$ ; \*\*\*,  $P < 0.001$ ).

endothelial polarity has recently proven to be a powerful tool to dissect the behavior of ECs during vessel regression (Franco et al., 2015, 2016). Our polarity analysis in vivo revealed a profound reduction of axial polarity in IFT88-deficient ECs precisely

in the vascular plexus region that experiences intermediate shear values and high levels of regression. Vessels experiencing the highest shear stress, specifically arteries, showed the most robust polarization against flow. This effect appears to



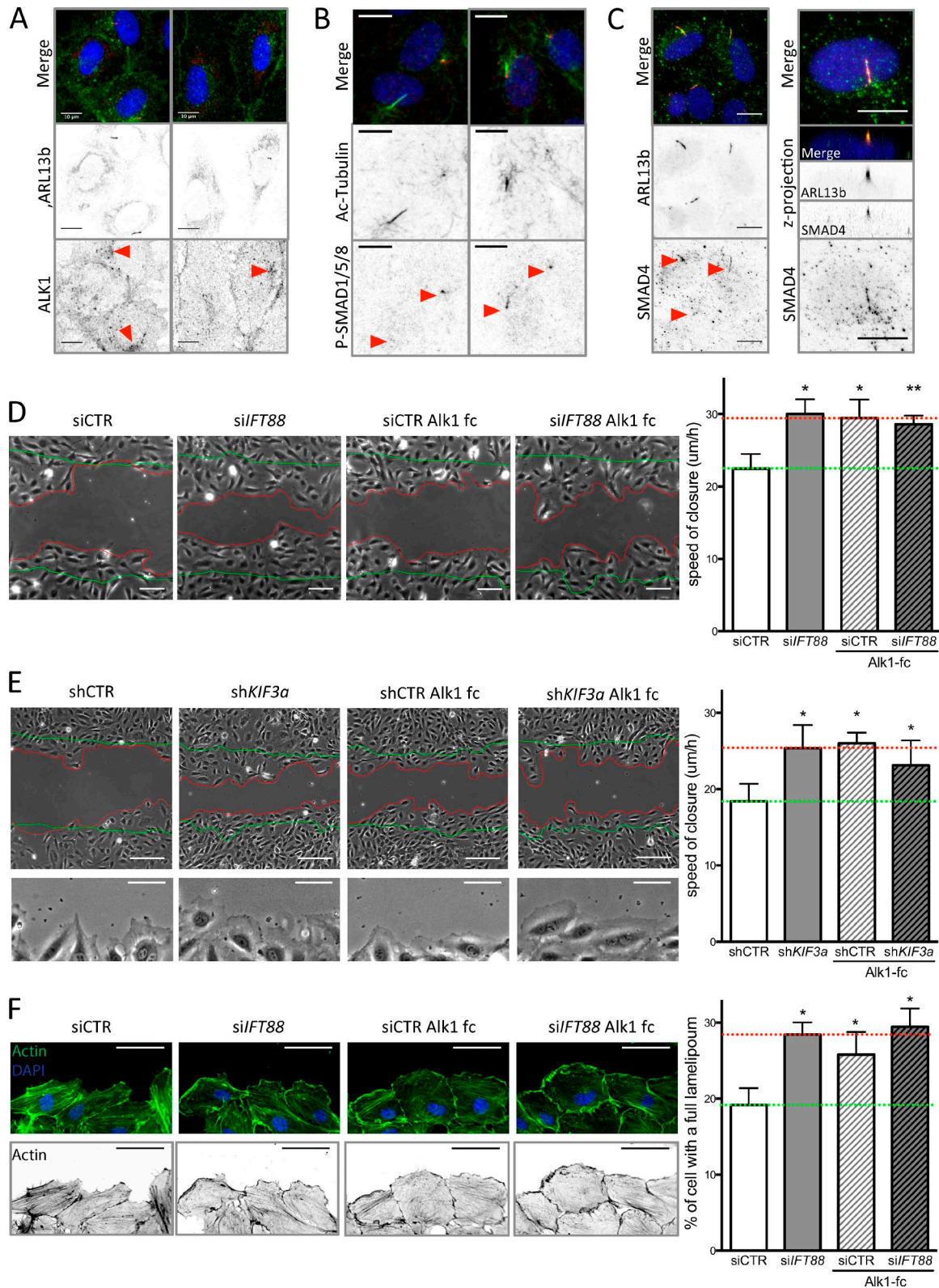


**Figure 5. Loss of BMP9 signaling through the cilium increases EC migration.** (A) HUVECs were stained for ARL13b (primary cilium; red), ALK1 (green), and DAPI (blue; methanol fixation,  $n = 2$ ) under static conditions. Bars, 10  $\mu\text{m}$ . (B) HUVECs were stained for acetylated tubulin (primary cilium; green), P-SMAD1/5/8 (red), and DAPI (blue; methanol fixation,  $n = 2$ ) under LSS conditions. Bars, 10  $\mu\text{m}$ . (C) HUVECs were stained for ARL13b (primary cilium; red), SMAD4 (green), and DAPI (blue; methanol fixation,  $n = 2$ ) under LSS conditions. Bars, 10  $\mu\text{m}$ . (D) A wound-closure assay was performed on ECs transfected with siCTR and siIFT88, treated or not with a BMP9 trap, an ALK1-Fc receptorbody (25 ng/ml, for the duration of the wound experiment). Representative images were taken 9 h after the wound was made (green lines, wound at  $t = 0$ ; red lines, wound at  $t = 9$  h) and the speed of closure was quantified ( $n = 5$ ; mean  $\pm$  SEM; two-sided

be independent of the primary cilium, as it is not expressed at these locations. Also, IFT88 mutants showed no change in axial polarity in ECs in areas exposed to HSS and displayed normal arterial morphologies.

Why then do some vessels lacking IFT88 show altered polarity and premature regression? The BMP-ALK1-SMAD pathway recently emerged as an important player in both endothelial flow responses and vessel stability. The complete loss of BMP9/10-ALK1 signaling reduces cellular quiescence in nascent vascular networks, resulting in dramatic hypersprouting (Larrivée et al., 2012), and triggers the formation of arteriovenous shunts (Laux et al., 2013; Baeyens et al., 2016b). In zebrafish embryos, ALK1 deficiency has been shown to drive shunt formation by impairing polarization and movement of ECs against flow (Rochon et al., 2016). Loss of the coreceptor Endoglin, a flow-sensitive enhancer of ALK1-BMP signaling (Baeyens et al., 2016b), also triggers arteriovenous shunts, but it does not mimic the excessive sprouting seen in ALK1 mutants (Jin et al., 2017). Interestingly, Endoglin profoundly increases EC SMAD1/5/8 phosphorylation through BMP9-mediated Alk1 activation, particularly under HSS (Baeyens et al., 2016b), and promotes EC migration against the flow (Jin et al., 2017). Our present work reinforces the idea that BMP9-ALK1-SMAD1/5/8 signaling is intimately connected with endothelial flow responses and polarized migration, but it suggests the existence of a tunable range of shear and BMP sensitivity involving distinct molecular mechanisms. Whereas Endoglin operates at high shear, we find that the cilium components IFT88 and KIF3a, and likely the cilium itself, confer a particular sensitivity to BMP9 at low shear levels. Given that arteriovenous shunts form in high-flow regions, the differential involvement of Endoglin and the cilium at high and low flow, respectively, may also explain why IFT88 deficiency does not cause shunt formation. Mechanistically, how SMAD signaling promotes endothelial polarity against flow remains unclear. Nevertheless, our data identify, for the first time in ECs, the presence of phosphorylated SMAD1/5/8 and SMAD4 along the primary cilium, a mechanosensitive structure that is linked to the polarized microtubular organization of the cell and its Golgi position. In human mesenchymal stem cells, phosphorylated SMAD2/3 was detected at the basal body of primary cilia, promoting signaling after TGF $\beta$  stimulation (Labour et al., 2016). In *Xenopus laevis* embryos, SMAD1 is recruited to the base of the cilium for degradation and signal termination (Fuentealba et al., 2007). In contrast, given that ALK1-Fc treatment mimics IFT88 or KIF3a depletion, our data point toward an activating process in ECs.

Interestingly, in IFT88-deficient ECs, p-SMAD1/5/8 levels were identical between ECs exposed to LSS and HSS, whereas nuclear localization was decreased only in LSS. This suggests that

the primary cilium, or IFT88, may also contribute to transport of p-SMAD1/5/8 to the nucleus. The microtubule motors Kinesin and Dynein actively transport SMADs to the activating receptor kinases at the membrane and to the nucleus, respectively, (Chen and Xu, 2011), and are also important for cilium-dependent mechanisms (Verhey et al., 2011). Our data showing identical effects of losing either of two unrelated essential components of the primary cilium, and of inhibiting BMP signaling on cell migration in vitro, together with the localization of BMP-ALK1-SMAD signals at the primary cilium, favor the idea that it is the primary cilium that mediates flow-dependent sensitization to BMP, thereby affecting cell rearrangements. Conceptually, our discovery of the primary cilium sensitizing ECs to the activity of BMP-ALK1-SMAD signaling at low shear levels, together with the earlier findings of Endoglin performing a similar function at high shear levels, suggest that critical endothelial responses to the changing hemodynamic conditions across the remodeling network are fine-tuned through the integration of mechanosensing and receptor kinases to ensure proper vascular patterning and flow distribution. How well and in which direction ECs polarize and migrate as flow response appear to take center stage in this morphogenic process. Future work will need to address how the primary cilium sensitizes ECs to BMP and what downstream effectors of BMP signaling are critical for cell polarization and stabilization of vessels during remodeling.

## Materials and methods

### Mice and treatments

The following mouse strains were used: C57/BL6J, *Ift88*<sup>fl</sup> (Haycraft et al., 2007), *Pdgfrb-iCre-ERT2-Egfp* (Claxton et al., 2008), and *R26mTmG* (Muzumdar et al., 2007). Mice were maintained at the Max Delbrück Center for Molecular Medicine under standard husbandry conditions. Tamoxifen (Sigma-Aldrich) was injected i.p. (20  $\mu$ g/g animal) at P1 and P3. Eyes were then collected at P4, P6, or P15 onwards. For C57/BL6J mice, eyes were collected at P3, P6, P11, and P15. For EC proliferation assessment in the retina, mouse pups were injected i.p. 2 h before collection of eyes with 20  $\mu$ l/g EdU solution (0.5 mg/ml; C10340; Invitrogen). Animal procedures were performed in accordance with the animal license IC113 G 0117/15. The investigators were blinded to allocation during experiments.

### Fish maintenance and stocks

Zebrafish (*Danio rerio*) were raised and staged as previously described (Kimmel et al., 1995). We used the double transgenic line Tg(kdr-l:ras-Cherry916;  $\beta$ -actin::arl13b-eGfp) by crossing two previously described fish lines (Borovina et al., 2010; Phng et

Wilcoxon test; \*,  $P < 0.05$ ; \*\*,  $P < 0.01$ ). Bars, 100  $\mu$ m. (E) A wound-closure assay was performed on ECs transfected with shCTR and shKIF3a, treated or not with ALK1-Fc (25 ng/ml, for the duration of the wound experiment). Representative images were taken 9 h after the wound was made (green lines, wound at  $t = 0$ ; red lines, wound at  $t = 9$  h) and the speed of closure was quantified ( $n = 7$ ; mean  $\pm$  SEM; two-sided Wilcoxon test; \*,  $P < 0.05$ ; \*\*,  $P < 0.01$ ). Bars, 150  $\mu$ m. Bottom images of the panel highlight lamellipodia formation in shKIF3a, ALK1-fc, and shKIF3a+ALK1-fc condition compared with control. Bars, 60  $\mu$ m. (F) Representative images of actin staining (phalloidin-Alexa Fluor 594; green, top panel; black, bottom panel) of the ECs leading the wound closure and quantification of the number of cell with an undisrupted front lamellipodium (observed after 6 h of wound;  $n = 3$ ; two-sided paired  $t$  test. Data distribution was assumed to be normal, but this was not formally tested. \*,  $P < 0.05$ . Bars, 60  $\mu$ m.



al., 2013). The  $\beta$ -actin::arl13b-eGFP line was a gift from B. Ciruna (University of Toronto, Toronto, Ontario, Canada).

#### Dynabead-mediated isolation of lung ECs from neonatal mice

Lungs of P6 mouse pups were removed, minced using a scalpel and digested with 2.2  $\mu$ g/ml Dispase in HBSS with calcium/magnesium for 60 min at 37°C. Digested tissues were homogenized using a P1000 pipette and filtrated through a 40- $\mu$ m cell strainer. After centrifugation, the cell suspension was incubated for 30 min at room temperature with 100  $\mu$ l magnetic Dynabeads (Invitrogen) that had been conjugated overnight with anti-mouse CD144 antibody in PBS/EDTA 0.5 mM and 0.5% BSA. Cells attached to the beads were collected using an MPC magnet (Invitrogen) and washed three times with PBS/EDTA 2 mM and 0.5% BSA. Collected cells were then plated on 0.5% gelatin-coated wells and treated with 1  $\mu$ M tamoxifen (every 2 d) to induce deletion once they reached confluency at P1.

#### Dynabead-mediated isolation of retinal ECs from neonatal mice

Eyes of P6 mouse pups were removed, dissected in DMEM, and digested with 1 mg/ml Collagenase-A for 10 min at 37°C. Digested tissues were filtrated through a 40- $\mu$ m cell strainer. The cell suspension was incubated for 20 min at 4°C with 10  $\mu$ l magnetic Dynabeads (Invitrogen) per retina that had been conjugated overnight with anti-mouse CD31 antibody in 0.5 mM PBS/EDTA and 0.1% BSA. Cells coated with beads were collected using an MPC magnet (Invitrogen) and washed three times with 0.5 mM PBS/EDTA and 0.1% BSA. Cells not coated with beads were collected as a negative control. Collected cells were then processed for RNA extraction.

#### Cell culture and microfluidic chamber experiments

HUVECs (passage 2 to 6; PromoCell) were routinely cultured in EBM-Bulletkit (Promocell). For siRNA experiments, HUVECs were transfected with ON-TARGET smart pool control nontargeting siRNAs (D-001210-02-20; Dharmacon) and siRNAs against human IFT88 (L-012281-01-0005, siRNA 1: 5'-GAGAAUUAUAUGAUCGUGA-3'; siRNA 2: 5'-AGGCCAAUGGAACGUGAAA-3', siRNA 3: 5'-AGGAAGUGCUAGCGGUGAU-3'; siRNA 4: 5'-AGUAAAGGU GAACGACUAA-3'; Dharmacon). HUVECs were transfected with 25 nM siRNA using Dharmafect 1 transfection reagent. In brief, siRNA and Dharmafect1 were diluted in Optimen medium in separated vials for 5 min and then carefully mixed. After 20 min, the mix was added to the cells. For static experiments, cells were used between 24 and 48 h after transfection. For flow experiments, cells were cultured on 0.2% gelatin-coated slides (Menzel Glaser), and unidirectional laminar shear stress was applied 36 h after transfection using peristaltic pumps (Gilson) connected to a glass reservoir (ELLIPSE) and the chamber containing the slide. Local shear stress was calculated using Poiseuille's law and averaged to 2 (LSS) or 20 dyn/cm<sup>2</sup> (HSS). Cells were exposed to shear stress for 45 min using EBM media (Promocell) and costimulated with 0, 5, 25, 100, 500, and 1,000 pg/ml BMP9 (3209-BP-010; R&D) under the different flow conditions for the dose-response experiment (Fig. 4 C and Fig. S3, D-F), with 10 pg/ml for staining (Fig. 4, D and E). For quantitative PCR under static conditions,

ECs were stimulated with 25 pg/ml BMP9 for 2 h. For wound assays, ECs were treated with 25 ng/ml Alk1-fc (R&D) or vehicle for the duration of the wound.

#### Adenoviral transduction

pENTR-Arl13b2 was a gift from T. Caspary (Emory University, Atlanta, GA; plasmid 40871; Addgene). The cDNA of mEGFP was inserted upstream of the Arl13b2 cDNA using the NEB Builder HiFi DNA Assembly system (New England Biolabs). Arl13b-mEGFP cDNA was then cloned into pAd/CMV/V5-DEST vector from the ViraPower Adenoviral Expression system (ThermoFisher Scientific). Replication-incompetent viral particles were produced in 293A cells following the manufacturer's instructions.

#### Lentiviral transduction

Lentivirus expressing inducible shRNA (Sigma-Aldrich) was used to silence Kinesin-like protein (KIF3A, shRNA sequence: 5'-CCGGCGTCAGTCTTTGATGAACTACTCGAGTAGTTTCATCA AAGACTGACGTTTTTG-3'). HUVECs were infected in the presence of hexadimethrine bromide (at 8  $\mu$ g/ml) with lentivirus at MOI 2.5. Negative controls were lentivirus expressing a nontarget shRNA used at the same MOI as for the protein of interest. Transduced cells were amplified and selected using puromycin (P9620; Sigma-Aldrich) at 1  $\mu$ g/ml during amplification. Puromycin treatment was stopped during experiments. shRNA expression was induced by treating HUVECs for 5 d using IPTG (I6758; Sigma-Aldrich) at 1 mmol/liter.

#### Western blotting

HUVECs were washed with cold PBS and scraped off in M-PER (Mammalian Protein Extraction Reagent; ThermoScientific) completed protease and phosphatase inhibitors (Roche). Lysates were centrifuged and protein supernatant was quantified using the Lowry protein assay (Bio-Rad). Lysates were mixed with reducing sample buffer for electrophoresis and subsequently transferred onto polyvinylidene fluoride membranes. Equal loading was checked using Ponceau red solution. Membranes were incubated with primary antibodies (see below). After incubation with secondary antibodies (1:3,000; GE Healthcare), immunodetection was performed using an enhanced chemiluminescence kit (SuperSignal West Dura; Pierce), and bands were revealed using the Las-4000 imaging system. After initial immunodetection, membranes were stripped of antibodies and reprobed with anti-GAPDH antibody. Values reported from Western blots were obtained by band density analysis using Image Gauge software (Fujifilm) and expressed as the ratio of the protein of interest to GAPDH. The following antibodies were used: GAPDH (ref MAB374, goat; 1:10,000; Millipore), IFT88 (ref 13967-1-AP, rabbit; 1:500; Proteintech), p-SMAD1/5/8 (ref 13820, rabbit; 1:500; CST), SMAD1 (ref 385400, rabbit; 1:500; CST).

#### Immunofluorescence staining

Eyes were collected and fixed with 4% PFA in PBS for 1 h at 4°C, and retinas were then dissected in PBS. Blocking/permeabilization was performed using Claudio's blocking buffer (CBB; Franco et al., 2013), consisting of 1% FBS (Gibco), 3% BSA (Sigma-Aldrich), 0.5% Triton X-100 (Sigma-Aldrich), 0.01% sodium deoxycholate



(Sigma-Aldrich), and 0.02% sodium azide (Sigma-Aldrich) in PBS at pH 7.4 for 1–2 h with rocking at 4°C. Primary antibodies were incubated at the desired concentration in 1:1 CBB/PBS with rocking at 4°C overnight and secondary antibodies were incubated at the desired concentration in 1:1 CBB/PBS for 2 h at room temperature. DAPI (Sigma-Aldrich) was used for nuclear labeling. Retinas were mounted on slides using Vectashield mounting medium (H-1000; Vector Labs).

HUVECs were fixed using 100% cold methanol for 10 min (for cilium staining) or PFA 4% for 10 min (for all other stainings) and washed three times in PBS. Cells were then stained for 2 h with primary antibodies in 1:1 CBB/PBS followed by incubation for 1 h with secondary antibodies in 1:1 CBB/PBS (see list below). DAPI (Sigma-Aldrich) was used for nuclear labeling. Cells were mounted in Mowiol.

The following antibodies were used *in vivo*: ARL13b (ref 17711-1-AP, rabbit; 1:500; Proteintech), cleaved caspase (ref 9661, rabbit; 1:200; CST), collagen IV (ref ab6586, rabbit; 1:200; Abcam), ERG (ref ab92513, rabbit; 1:1,000; Abcam), GOLPH4 (ref ab28049, rabbit; 1:500; Abcam), ICAM2 (ref 553326, rat; 1:200; BD Biosciences), p-SMAD1/5/8 (rabbit; 1:200; CST; ref 13820), vascular endothelial (VE)-cadherin (ref 555289; rat; 1/100; BD Biosciences), Isolectin 488 (ref [I21411](#), 1:400; Invitrogen), and Isolectin 568 (ref [I21412](#), 1:400; Invitrogen). The following antibodies were used *in vitro*: acetylated tubulin (ref T6793, rabbit; 1:500; Sigma-Aldrich), ALK1 (ref AF370, goat; 1:500; R&D), detyrosinated tubulin (ref AB3201, rabbit; 1:500; Millipore), p-SMAD1/5/8 (ref 13820, rabbit; 1:500; CST), SMAD4 (ref sc-7966, rabbit; 1:500; Santa Cruz), p-SMAD1/5/8 (ref 13820, rabbit; 1:500; CST), VE-cadherin (ref sc-6458, goat; 1:100; Santa Cruz), and Phalloidin 568 (ref A12380, 1:100; Invitrogen).

## Microscope image acquisition

### Retina imaging

Images of retinas were taken using a LSM 780 inverted microscope (Zeiss) equipped with a Plan-Apochromat 20×/0.8 NA Ph2 objective or with a Plan-Apochromat 63×/1.4 NA DIC objective or using a LSM 700 upright microscope (Zeiss) equipped with a Plan-Apochromat 20×/0.8 NA Ph2 objective. Both microscopes were equipped with a photon multiplier tube detector. Images were taken at room temperature using Zen 2.3 software (Zeiss).

### In vitro imaging

Images from fluorescently labeled HUVECs were acquired using a LSM 700 upright microscope equipped with a Plan-Apochromat 20×/0.8 NA Ph2 objective. Images were taken at room temperature using Zen 2.3 software.

Bright-field images were taken using a Leica DMIL LED microscope equipped with a 10×/0.22 NA Ph1 objective and a CCD camera (DFC3000 G). Images were acquired at room temperature while the cells were still in their culture medium using LAS X software (Leica).

### Live-cell imaging

HUVEC cells were plated in ibidi slides 0.6 and infected with the Arl13b2-mEGFP virus. 48 h later, cells were stained with 1 μM siR-DNA nuclear dye (Spirochrome) and incubated for an additional

hour. Cells were subsequently imaged using an LSM 780 inverted microscope (Zeiss) equipped with Plan-Apochromat 20×/0.8 NA Ph2 objective and the Definite Focus system. Time series of single planes were acquired at five randomly selected positions with 5 min resolution, 0.42 × 0.42 μm pixel, and an open pinhole. Images were taken at 37°C, 5% CO<sub>2</sub> using Zen 2.3 software. Images were analyzed in Fiji ([Schindelin et al., 2012](#)).

### Zebrafish live imaging

Zebrafish embryos (24–30 hpf) were dechorionated, anaesthetized with 0.16 mg/ml Tricaine methanesulfonate (Sigma-Aldrich), mounted in 0.8% low-melting-point agarose (Life Technologies), and immersed in E3 buffer with 1× Tricaine for image acquisition. Live imaging was performed on a Yokogawa CSU-W1 upright 3i spinning-disc confocal microscope using a Zeiss Plan-Apochromat 63×/1.0 NA water-dipping objective and a CMOS [C11440](#)-22cu camera (Hamamatsu Photonics). Images were acquired using SlideBook 6 at a constant temperature of 28°C.

### Image analysis

*In vivo*, the primary cilia belonging to ECs were identified as finger-like structures close to endothelial nuclei and localized inside the vessel (luminal side of Isolectin- or VE-cadherin-stained ECs). Veins and arteries of the retinal vasculature were identified based on their distinct morphological characteristics, with arteries showing dichotomous branching and a capillary free zone and veins appearing wider and mostly unbranched, surrounded by dense plexus. For quantifying the endothelial cilium in the IEC-IFT88 retinas, primary cilia were quantified only in veins, where their density was the highest in the control retinas. The few residual endothelial primary cilium appeared distributed along the vein. Lumen collapses were identified as ICAM2-negative/Isolectin-positive vessel segments; empty sleeves were identified as Collagen IV-positive/Isolectin-negative vessel segments. EdU-positive ECs were identified as cells positive for both ERG and EdU. EC density was assessed in the remodeling plexus and quantified as number of ECs per field of view. *In vitro*, the primary cilium was identified as a finger-like structure protruding above the cell and either close to the nucleus or on top of the Golgi apparatus. Translocation of p-SMAD to the nucleus was quantified using Cellprofiler (Broad Institute). In brief, nuclei were segmented based on the DAPI staining, and the nuclear signal measured. For all animal experiments, experimenters were unaware of the genotypes of the animals while acquiring images. For zebrafish experiments, images were analyzed using Fiji software. Z-stacks and time-lapse sequences were first flattened by maximum intensity projection. XY drift was corrected using the MultiStackReg plugin (B. Busse, National Institute of Child Health and Human Development, Bethesda, MD). Fluorescence bleaching was corrected by histogram matching.

### Arteriovenous coordinate system

To characterize the position of events and structures within a mouse retina, we introduced a vein–artery coordinate system, which characterizes the relative position in the mouse retina

with respect to the closest distance to arteries and veins. To obtain this coordinate system, the position of the midlines of the 2D projections of veins and arteries were identified manually in images of quarters of the retinas. For each point in the image, the closest distance to any vein and artery are given by  $d_v$  and  $d_a$ , respectively, and the corresponding arteriovenous distance is thus defined by

$$d_v/d_a + d_a.$$

It is 0 on veins and 1 on arteries and scales linearly between veins and arteries. The positions of empty collagen sleeves (Fig. 3, E and F) and divergent regions (Fig. 4, E and F) were analyzed within this coordinate system.

### Mouse retina rheology model

Analysis of the axial polarity of ECs was performed by measuring the angle formed by the nucleus–Golgi axis and the flow direction using a mouse retina rheology model (Bernabeu et al., 2014). In brief, retinal vascular plexuses were stained for ICAM2 and imaged following the previously mentioned protocol. The resulting images were postprocessed in ImageJ to isolate the luminal region of interest, which was further processed with MATLAB (MathWorks) to extract the image skeleton and compute vessel radii along the network. Based on the computed image skeleton and radii, a 3D triangulation of the plexus luminal surface was generated with VMTK (Orobix srl). The computational fluid dynamics software package HemeLB (Bernabeu et al., 2014) was used to compute high-resolution estimates of pressure, velocity, and shear stress across the domain. Shear stress values obtained from simulation are impacted by the choice of inlet/outlet boundary conditions on the simulated hemodynamics. Ideally, one would use experimental measurements of flow rate and/or pressure to close the system. We could not obtain these data experimentally and relied on the data surveyed in Bernabeu et al. (2014) obtained from adult animals. Therefore, shear stress values in Fig. 4 C are theoretical values bound to our specific settings. Flow visualization was generated with Paraview (Kitware), and postprocessing of the results was performed with custom-made MATLAB scripts.

### Flow-induced polarity analysis

To analyze the coupling between the polarization of cells (given by the Golgi–nucleus orientation) and the local direction and velocity of blood flow (obtained by the polnet analysis), we averaged the angles between flow and cell orientation after the binning with the local blood velocity. A deviation of 0 corresponds to the case where the Golgi–nucleus vector is opposite to the blood flow, whereas a deviation of  $\pi$  corresponds to the vectors being in the same direction as the blood flow. Thus, if all cells at a given flow velocity were perfectly polarized against the flow, the mean deviation would be 0; if they were all polarized with the flow, the mean deviation would be  $\pi$ ; and if they were randomly polarized, one would expect to find the mean deviation to be  $\pi/2$ .

### Cell cycle analysis of ECs from retinas

Eyes of P6 *Ift88*<sup>fl/fl</sup>; *Pdgfrb-iCre-ERT2-Egfp*<sup>Tg/wt</sup>; *R26-mTmG*<sup>Tg/Tg</sup> or *Pdgfrb-iCre-ERT2-Egfp*<sup>Tg/wt</sup>; *R26-mTmG*<sup>Tg/Tg</sup> mouse pups were

collected, dissected in DMEM, and digested with 1 mg/ml Collagenase-A for 10 min at 37°C. Digested tissues were filtrated through a 40- $\mu$ m cell strainer, centrifuged and fixed with cold 100% methanol. Cells were stored in 90% methanol at –80°C before being further processed. Cells were then centrifuged to remove methanol and resuspended in PI/RNase staining solution (Cell Signaling) for 30 min before analysis by flow cytometry (LSRII; BD). In brief, ECs were identified as GFP positive, cell doublets were excluded, and the cell cycle was analyzed in the phycoerythrin channel. Acquisition was done using DIVA software and analysis using Flow-Jo software.

### Wound-closure assay

Previously transfected cells were passed into wound-healing assay culture insert (ibidi) 24 h after transfection. After 24 h of culture in the device, the insert was removed to make a wound of ~450  $\mu$ m. Images were taken at three different locations along the wound at every hour for 9 h. The distance between both sides of the wound was measured to calculate the speed of closure over the 9 h. For staining experiments, cells were fixed 6 h after removing the insert.

### RNA extraction and real-time quantitative RT-PCR

RNA was extracted and purified using the Qiagen RNeasy kit following the manufacturer's instructions for the experiment under static conditions or using Trizol and the Direct-zol RNA kit (zyzo research) for experiments under flow. After measuring concentration and purity, RNA was kept at –80°C before use. RT-PCR was performed with 0.5  $\mu$ g RNA using QIAGEN products and protocols; quantitative PCR was performed using Taqman products and protocols. A set of three housekeeping genes was selected for both human and mouse samples. Normalization was done using the 2 $\Delta\Delta$ CT method.

The following human Taqman probes were used: *ID1* (Hs03676575), *SMAD6* (Hs00178579), *SERPINI* (Hs01126606), *IFT88* (Hs00167926), *PTCH1* (Hs00121117), *GLII* (Hs00171790), *KIF3a* (Hs00199901), *AXIN2* (Hs00610344), *HES1* (Hs00172878), *UBC* (Hs01060665), and *HPRT* (Hs02800695). The following mouse Taqman probes were used: *Ift88* (Mm01313467), *Smad6* (Mm00484738), *Serpini* (Mm00435858), *Glii* (Mm00494654), *Cdh5* (Mm00486938), *Gapd* (Mm00484668), *Ubc* (Mm01201237), and *Hprt* (Mm03024075).

### Statistical analysis

Statistical analysis was performed using GraphPad Prism software. For in vivo experiments, two-sided Mann–Whitney *t* tests (unpaired, nonparametric) or two-way ANOVAs (data distribution was assumed to be normal, but this was not formally tested) were used. For in vitro experiments, two-sided Wilcoxon *t* tests (paired, nonparametric) were used, except for p-SMAD translocation, where a two-sided Mann–Whitney *t* test was used, and for the lamellipodia quantification, were a two-sided paired *t* test was used (data distribution was assumed to be normal, but this was not formally tested). Details of the statistical test used or each experiment can be found in the figure legends. The investigators were blinded to genotype during experiments and quantification.

## Online supplemental material

Fig. S1 shows the dynamic formation and retraction of cilia in ECs in vitro. Additionally, it provides evidence for efficient silencing of IFT88 in vivo both at the RNA and protein level, as well as for the loss of endothelial cilia. IFT88 iEC-KO retina displayed a normal vasculature at P15, suggesting recovery from the earlier developmental defect. Fig. S2 shows the results of flow cytometry, cleaved caspase-3, and EdU stainings of retinas, together demonstrating that cell cycle or apoptosis changes are unlikely the drivers of altered vascular density in cilia mutants. It also provides a visual explanation of the in silico flow modeling and the corresponding polarity analysis. Fig. S3 provides evidence for IFT88 and KIF3a silencing efficiency in vitro, additional graphic presentation for the dose-response curves of ECs to BMP9 stimulation, and a table of EC50 values. Quantitative PCR results show that silencing KIF3a also affects the BMP response of ECs. Video 1 shows that endothelial cilia are luminal and dynamic in the zebrafish embryo. Video 2: shows endothelial cilium formation in a zebrafish embryo. Video 3 shows endothelial cilium retraction in a zebrafish embryo. Video 4 shows endothelial cilia dynamics in vitro.

## Acknowledgments

We thank Dr. Veronique Gebala and Dr. Andre Rosa for helpful comments on the manuscript. We also thank Francois Billeaud for realization of the cartoon of the summary schematic.

This work was supported by the Britain Israel Research and Academic Exchange Partnership (A.-C. Vion and H. Gerhardt), the German Centre for Cardiovascular Research, the German Ministry of Education and Research (A.-C. Vion and A. Klaus-Bergmann), and European Research Council consolidator grant 311719 Reshape (H. Gerhardt). A. Szymborska was supported by European Molecular Biology Organization long-term fellowship ALTF 2014-1625. P.-E. Rautou was funded by the Agence Nationale pour la Recherche (grants ANR-14-CE12-0011, ANR-14-CE35-0022, and ANR-16-CE14-0015-01). M.O. Bernabeu was supported by the UK Engineering and Physical Sciences Research Council under the project "UK Consortium on Mesoscale Engineering Sciences" (grant EP/L00030X/1). This work used the ARCHER UK National Supercomputing Service (<http://www.archer.ac.uk>).

The authors declare no competing financial interests.

Author contributions: A.-C. Vion designed the study, performed experiments, analyzed the results, and wrote the manuscript. T. Zheng, T. Perovic, and A. Klaus-Bergmann performed experiments and analyzed the results. A. Hamouten, A. Szymborska, E. Bartels-Klein, and I. Hollfinger performed experiments. S. Alt performed quantitative analysis, analyzed results, and reviewed the manuscript. P.-E. Rautou provided reagents and reviewed the manuscript; M.O. Bernabeu performed experiments and reviewed the manuscript; H. Gerhardt designed the study and wrote the manuscript.

Submitted: 27 June 2017

Revised: 1 July 2017

Accepted: 30 January 2018

## References

- Baeyens, N., S. Nicoli, B.G. Coon, T.D. Ross, K. Van den Dries, J. Han, H.M. Lauridsen, C.O. Mejean, A. Eichmann, J.L. Thomas, et al. 2015. Vascular remodeling is governed by a VEGFR3-dependent fluid shear stress set point. *eLife*. 4: e04645. <https://doi.org/10.7554/eLife.04645>
- Baeyens, N., C. Bandyopadhyay, B.G. Coon, S. Yun, and M.A. Schwartz. 2016a. Endothelial fluid shear stress sensing in vascular health and disease. *J. Clin. Invest.* 126:821–828. <https://doi.org/10.1172/JCI83083>
- Baeyens, N., B. Larrivée, R. Ola, B. Hayward-Piatkowski, A. Dubrac, B. Huang, T.D. Ross, B.G. Coon, E. Min, M. Tsarfati, et al. 2016b. Defective fluid shear stress mechanotransduction mediates hereditary hemorrhagic telangiectasia. *J. Cell Biol.* 214:807–816. <https://doi.org/10.1083/jcb.201603106>
- Bernabeu, M.O., M.L. Jones, J.H. Nielsen, T. Krüger, R.W. Nash, D. Groen, S. Schmieschek, J. Hetherington, H. Gerhardt, C.A. Franco, and P.V. Coveney. 2014. Computer simulations reveal complex distribution of haemodynamic forces in a mouse retina model of angiogenesis. *J. R. Soc. Interface*. 11:11. <https://doi.org/10.1098/rsif.2014.0543>
- Bernabeu, M.O., Jones, M.L., Nash, R.W., Pezzarossa, A., Coveney, P.V., Gerhardt, H., and Franco, C.A. PolNet Analysis: a software tool for the quantification of network-level endothelial cell polarity and blood flow during vascular remodelling. *bioRxiv*. doi: <https://doi.org/10.1101/237602> (Preprint posted December 22, 2017)
- Boehlke, C., F. Kotsis, B. Buchholz, C. Powelske, K.U. Eckardt, G. Walz, R. Nitschke, and E.W. Kuehn. 2013. Kif3a guides microtubular dynamics, migration and lumen formation of MDCK cells. *PLoS One*. 8:e62165. <https://doi.org/10.1371/journal.pone.0062165>
- Boehlke, C., H. Janusch, C. Hamann, C. Powelske, M. Mergen, H. Herbst, F. Kotsis, R. Nitschke, and E.W. Kuehn. 2015. A Cilia Independent Role of Ift88/Polaris during Cell Migration. *PLoS One*. 10:e0140378. <https://doi.org/10.1371/journal.pone.0140378>
- Borovina, A., and B. Ciruna. 2013. IFT88 plays a cilia- and PCP-independent role in controlling oriented cell divisions during vertebrate embryonic development. *Cell Rep.* 5:37–43. <https://doi.org/10.1016/j.celrep.2013.08.043>
- Borovina, A., S. Superina, D. Voskas, and B. Ciruna. 2010. Vangl2 directs the posterior tilting and asymmetric localization of motile primary cilia. *Nat. Cell Biol.* 12:407–412. <https://doi.org/10.1038/ncb2042>
- Chen, X., and L. Xu. 2011. Mechanism and regulation of nucleocytoplasmic trafficking of smad. *Cell Biosci.* 1:40. <https://doi.org/10.1186/2045-3701-1-40>
- Chen, Q., L. Jiang, C. Li, D. Hu, J.W. Bu, D. Cai, and J.L. Du. 2012. Haemodynamics-driven developmental pruning of brain vasculature in zebrafish. *PLoS Biol.* 10:e1001374. <https://doi.org/10.1371/journal.pbio.1001374>
- Claxton, S., V. Kostourou, S. Jadeja, P. Chambon, K. Hodivala-Dilke, and M. Fruttiger. 2008. Efficient, inducible Cre-recombinase activation in vascular endothelium. *Genesis*. 46:74–80. <https://doi.org/10.1002/dvg.20367>
- Culver, J.C., and M.E. Dickinson. 2010. The effects of hemodynamic force on embryonic development. *Microcirculation*. 17:164–178. <https://doi.org/10.1111/j.1549-8719.2010.00025.x>
- Delaval, B., A. Bright, N.D. Lawson, and S. Doherty. 2011. The cilia protein IFT88 is required for spindle orientation in mitosis. *Nat. Cell Biol.* 13:461–468. <https://doi.org/10.1038/ncb2202>
- Dinsmore, C., and J.F. Reiter. 2016. Endothelial primary cilia inhibit atherosclerosis. *EMBO Rep.* 17:156–166. <https://doi.org/10.15252/embr.201541019>
- Dolan, J.M., J. Kolega, and H. Meng. 2013. High wall shear stress and spatial gradients in vascular pathology: a review. *Ann. Biomed. Eng.* 41:1411–1427. <https://doi.org/10.1007/s10439-012-0695-0>
- Egorova, A.D., P.P. Khedoe, M.J. Goumans, B.K. Yoder, S.M. Nauli, P. ten Dijke, R.E. Poelmann, and B.P. Hierck. 2011. Lack of primary cilia primes shear-induced endothelial-to-mesenchymal transition. *Circ. Res.* 108:1093–1101. <https://doi.org/10.1161/CIRCRESAHA.110.231860>
- Franco, C.A., J. Blanc, A. Parlakian, R. Blanco, I.M. Aspalter, N. Kazakova, N. Digué, E. Mylonas, J. Gao-Li, A. Vahtokari, et al. 2013. SRF selectively controls tip cell invasive behavior in angiogenesis. *Development*. 140:2321–2333. <https://doi.org/10.1242/dev.091074>
- Franco, C.A., M.L. Jones, M.O. Bernabeu, I. Geudens, T. Mathivet, A. Rosa, F.M. Lopes, A.P. Lima, A. Ragab, R.T. Collins, et al. 2015. Dynamic endothelial cell rearrangements drive developmental vessel regression. *PLoS Biol.* 13:e1002125. <https://doi.org/10.1371/journal.pbio.1002125>
- Franco, C.A., M.L. Jones, M.O. Bernabeu, A.C. Vion, P. Barbacena, J. Fan, T. Mathivet, C.G. Fonseca, A. Ragab, T.P. Yamaguchi, et al. 2016. Non-canonical Wnt signalling modulates the endothelial shear stress flow



- sensor in vascular remodelling. *eLife*. 5:e07727. <https://doi.org/10.7554/eLife.07727>
- Fuentealba, L.C., E. Eivers, A. Ikeda, C. Hurtado, H. Kuroda, E.M. Pera, and E.M. De Robertis. 2007. Integrating patterning signals: Wnt/GSK3 regulates the duration of the BMP/Smad1 signal. *Cell*. 131:980–993. <https://doi.org/10.1016/j.cell.2007.09.027>
- Gerhardt, C., T. Leu, J.M. Lier, and U. R  ther. 2016. The cilia-regulated proteasome and its role in the development of ciliopathies and cancer. *Cilia*. 5:14. <https://doi.org/10.1186/s13630-016-0035-3>
- Givens, C., and E. Tzima. 2016. Endothelial Mechanosignaling: Does One Sensor Fit All? *Antioxid. Redox Signal*. 25:373–388. <https://doi.org/10.1089/ars.2015.6493>
- Goetz, S.C., and K.V. Anderson. 2010. The primary cilium: a signalling centre during vertebrate development. *Nat. Rev. Genet.* 11:331–344. <https://doi.org/10.1038/nrg2774>
- Goetz, J.G., E. Steed, R.R. Ferreira, S. Roth, C. Ramsbacher, F. Boselli, G. Charvin, M. Liebling, C. Wyart, Y. Schwab, and J. Vermot. 2014. Endothelial cilia mediate low flow sensing during zebrafish vascular development. *Cell Rep.* 6:799–808. <https://doi.org/10.1016/j.celrep.2014.01.032>
- Guo, X., and X.F. Wang. 2009. Signaling cross-talk between TGF-beta/BMP and other pathways. *Cell Res.* 19:71–88. <https://doi.org/10.1038/cr.2008.302>
- Haycraft, C.J., Q. Zhang, B. Song, W.S. Jackson, P.J. Detloff, R. Serra, and B.K. Yoder. 2007. Intraflagellar transport is essential for endochondral bone formation. *Development*. 134:307–316. <https://doi.org/10.1242/dev.02732>
- Hori, Y., T. Kobayashi, Y. Kikko, K. Kontani, and T. Katada. 2008. Domain architecture of the atypical Arf-family GTPase Arl13b involved in cilia formation. *Biochem. Biophys. Res. Commun.* 373:119–124. <https://doi.org/10.1016/j.bbrc.2008.06.001>
- Iomini, C., K. Tejada, W. Mo, H. Vaananen, and G. Piperno. 2004. Primary cilia of human endothelial cells disassemble under laminar shear stress. *J. Cell Biol.* 164:811–817. <https://doi.org/10.1083/jcb.200312133>
- Isogai, S., N.D. Lawson, S. Torrealday, M. Horiguchi, and B.M. Weinstein. 2003. Angiogenic network formation in the developing vertebrate trunk. *Development*. 130:5281–5290. <https://doi.org/10.1242/dev.00733>
- Jin, Y., L. Muhl, M. Burmakin, Y. Wang, A.C. Duchez, C. Betsholtz, H.M. Arthur, and L. Jakobsson. 2017. Endoglin prevents vascular malformation by regulating flow-induced cell migration and specification through VEGFR2 signalling. *Nat. Cell Biol.* 19:639–652. <https://doi.org/10.1038/ncb3534>
- Jones, C., V.C. Roper, I. Foucher, D. Qian, B. Banizs, C. Petit, B.K. Yoder, and P. Chen. 2008. Ciliary proteins link basal body polarization to planar cell polarity regulation. *Nat. Genet.* 40:69–77. <https://doi.org/10.1038/ng.2007.54>
- Kallakuri, S., J.A. Yu, J. Li, Y. Li, B.M. Weinstein, S. Nicoli, and Z. Sun. 2015. Endothelial cilia are essential for developmental vascular integrity in zebrafish. *J. Am. Soc. Nephrol.* 26:864–875. <https://doi.org/10.1681/ASN.2013121314>
- Kimmel, C.B., W.W. Ballard, S.R. Kimmel, B. Ullmann, and T.F. Schilling. 1995. Stages of embryonic development of the zebrafish. *Dev. Dyn.* 203:253–310. <https://doi.org/10.1002/aja.1002030302>
- Labour, M.N., M. Riffault, S.T. Christensen, and D.A. Hoey. 2016. TGF  1-induced recruitment of human bone mesenchymal stem cells is mediated by the primary cilium in a SMAD3-dependent manner. *Sci. Rep.* 6:35542. <https://doi.org/10.1038/srep35542>
- Larriv  e, B., C. Prahst, E. Gordon, R. del Toro, T. Mathivet, A. Duarte, M. Simons, and A. Eichmann. 2012. ALK1 signaling inhibits angiogenesis by cooperating with the Notch pathway. *Dev. Cell*. 22:489–500. <https://doi.org/10.1016/j.devcel.2012.02.005>
- Laux, D.W., S. Young, J.P. Donovan, C.J. Mansfield, P.D. Upton, and B.L. Roman. 2013. Circulating Bmp10 acts through endothelial Alk1 to mediate flow-dependent arterial quiescence. *Development*. 140:3403–3412. <https://doi.org/10.1242/dev.095307>
- Lee, J., A. Ishihara, and K. Jacobson. 1993. The fish epidermal keratocyte as a model system for the study of cell locomotion. *Symp. Soc. Exp. Biol.* 47:73–89.
- Liu, J., Y. Wang, Y. Akamatsu, C.C. Lee, R.A. Stetler, M.T. Lawton, and G.Y. Yang. 2014. Vascular remodeling after ischemic stroke: mechanisms and therapeutic potentials. *Prog. Neurobiol.* 115:138–156. <https://doi.org/10.1016/j.pneurobio.2013.11.004>
- Muzumdar, M.D., B. Tasic, K. Miyamichi, L. Li, and L. Luo. 2007. A global double-fluorescent Cre reporter mouse. *Genesis*. 45:593–605. <https://doi.org/10.1002/dvg.20335>
- Nauli, S.M., Y. Kawanabe, J.J. Kaminski, W.J. Pearce, D.E. Ingber, and J. Zhou. 2008. Endothelial cilia are fluid shear sensors that regulate calcium signaling and nitric oxide production through polycystin-1. *Circulation*. 117:1161–1171. <https://doi.org/10.1161/CIRCULATIONAHA.107.710111>
- Nonaka, S., Y. Tanaka, Y. Okada, S. Takeda, A. Harada, Y. Kanai, M. Kido, and N. Hirokawa. 1998. Randomization of left-right asymmetry due to loss of nodal cilia generating leftward flow of extraembryonic fluid in mice lacking KIF3B motor protein. *Cell*. 95:829–837. [https://doi.org/10.1016/S0092-8674\(00\)81705-5](https://doi.org/10.1016/S0092-8674(00)81705-5)
- Ostrowski, M.A., N.F. Huang, T.W. Walker, T. Verwijlen, C. Poplawski, A.S. Khoo, J.P. Cooke, G.G. Fuller, and A.R. Dunn. 2014. Microvascular endothelial cells migrate upstream and align against the shear stress field created by impinging flow. *Biophys. J.* 106:366–374. <https://doi.org/10.1016/j.bpj.2013.11.4502>
- Pedersen, L.B., J.B. Mogenssen, and S.T. Christensen. 2016. Endocytic Control of Cellular Signaling at the Primary Cilium. *Trends Biochem. Sci.* 41:784–797. <https://doi.org/10.1016/j.tibs.2016.06.002>
- Phng, L.K., F. Stanchi, and H. Gerhardt. 2013. Filopodia are dispensable for endothelial tip cell guidance. *Development*. 140:4031–4040. <https://doi.org/10.1242/dev.097352>
- Potente, M., H. Gerhardt, and P. Carmeliet. 2011. Basic and therapeutic aspects of angiogenesis. *Cell*. 146:873–887. <https://doi.org/10.1016/j.cell.2011.08.039>
- Rochon, E.R., P.G. Menon, and B.L. Roman. 2016. Alk1 controls arterial endothelial cell migration in lumenized vessels. *Development*. 143:2593–2602. <https://doi.org/10.1242/dev.135392>
- Satir, P., L.B. Pedersen, and S.T. Christensen. 2010. The primary cilium at a glance. *J. Cell Sci.* 123:499–503. <https://doi.org/10.1242/jcs.050377>
- Schindelin, J., I. Arganda-Carreras, E. Frise, V. Kaynig, M. Longair, T. Pietzsch, S. Preibisch, C. Rueden, S. Saalfeld, B. Schmid, et al. 2012. Fiji: an open-source platform for biological-image analysis. *Nat. Methods*. 9:676–682. <https://doi.org/10.1038/nmeth.2019>
- Taulet, N., B. Vitre, C. Anguille, A. Douanier, M. Rocancourt, M. Taschner, E. Lorentzen, A. Echard, and B. Delaval. 2017. IFT proteins spatially control the geometry of cleavage furrow ingression and lumen positioning. *Nat. Commun.* 8:1928. <https://doi.org/10.1038/s41467-017-01479-3>
- Taulman, P.D., C.J. Haycraft, D.F. Balkovetz, and B.K. Yoder. 2001. Polaris, a protein involved in left-right axis patterning, localizes to basal bodies and cilia. *Mol. Biol. Cell*. 12:589–599. <https://doi.org/10.1091/mbc.12.3.589>
- Ten Dijke, P., A.D. Egorova, M.J. Goumans, R.E. Poelmann, and B.P. Hierck. 2012. TGF-   signaling in endothelial-to-mesenchymal transition: the role of shear stress and primary cilia. *Sci. Signal*. 5:pt2. <https://doi.org/10.1126/scisignal.2002722>
- Traub, O., and B.C. Berk. 1998. Laminar shear stress: mechanisms by which endothelial cells transduce an atheroprotective force. *Arterioscler. Thromb. Vasc. Biol.* 18:677–685. <https://doi.org/10.1161/01.ATV.18.5.677>
- Udan, R.S., T.J. Vadakkan, and M.E. Dickinson. 2013. Dynamic responses of endothelial cells to changes in blood flow during vascular remodeling of the mouse yolk sac. *Development*. 140:4041–4050. <https://doi.org/10.1242/dev.096255>
- Verhey, K.J., J. Dishinger, and H.L. Kee. 2011. Kinesin motors and primary cilia. *Biochem. Soc. Trans.* 39:1120–1125. <https://doi.org/10.1042/BST0391120>
- Vyalov, S., B.L. Langille, and A.I. Gotlieb. 1996. Decreased blood flow rate disrupts endothelial repair in vivo. *Am. J. Pathol.* 149:2107–2118.
- Wang, C., B.M. Baker, C.S. Chen, and M.A. Schwartz. 2013. Endothelial cell sensing of flow direction. *Arterioscler. Thromb. Vasc. Biol.* 33:2130–2136. <https://doi.org/10.1161/ATVBAHA.113.301826>
- Zhou, J., P.L. Lee, C.S. Tsai, C.I. Lee, T.L. Yang, H.S. Chuang, W.W. Lin, T.E. Lin, S.H. Lim, S.Y. Wei, et al. 2012. Force-specific activation of Smad1/5 regulates vascular endothelial cell cycle progression in response to disturbed flow. *Proc. Natl. Acad. Sci. USA*. 109:7770–7775. <https://doi.org/10.1073/pnas.1205476109>